ACS OMEGA

http://pubs.acs.org/journal/acsodf

Article

Late Cretaceous-Paleogene Exhumation History and Evolution of Paleotopography in the Gaize Basin, Central Tibet

Yuan Gao, Wentian Mi,* Wenguang Yang, Guozhong Ji, Yuhang Luo, and Ke Miao

Cite This: *ACS Omega* 2025, 10, 22562−22575

ABSTRACT: A series of terrestrial sedimentary basins along the Bangong-Nujiang Suture Zone (BNSZ) record a wealth of information regarding the uplift and geomorphological evolution of the central Tibetan Plateau. The uplift, exhumation, and sedimentation processes in these basins and the surrounding orogenic belts are of significant scientific importance for understanding the tectonic evolution of the central Tibetan Plateau. Taking the Gaize Basin as the research focus, low-temperature thermochronology and thermal history modeling were conducted on sandstone samples to analyze their exhumation history and driving mechanisms during the Late Cretaceous to Paleogene. Based on stratigraphy and the youngest detrital zircon ages, the samples were collected from the Upper Jurassic to Lower Cretaceous Shamuluo Formation; thermal history modeling using apatite and zircon (U−Th)/He (AHe/ZHe) results reveals two significant exhumation events: 87−70 and 56−26 Ma. The rapid cooling−exhumation event during the Late Cretaceous is associated with crustal shortening and thickening caused by the collision of the Lhasa-Qiangtang terrane; the Paleogene exhumation event is linked to tectonic uplift driven by the India-Asia collision and the continued northward subduction of the Indian continent. Continuous thrusting and uplift on both sides of the basin strengthened river cutting and erosion and gradually converted the external drainage system to an internal drainage system, and the high-relief terrain was progressively leveled and filled. The height of the surface uplift brought on by sediment accumulation was approximately 0.4 km. After Oligocene, high-altitude, low-relief terrain had already been established.

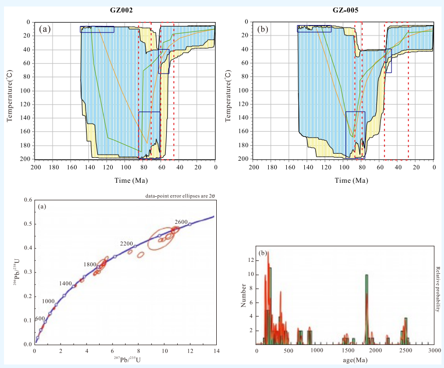

1. INTRODUCTION

The central Tibetan Plateau not only functions as a natural laboratory for probing into the plateau uplift but also presents itself as an outstanding venue for examining the coupling among various geospheres within the Earth's science system. Furthermore, the majority of the Tibetan Plateau is distinguished by its low-relief topography and high-altitude characteristics.[1−7] The BNSZ spans across the central Tibetan Plateau, featuring multiple Cenozoic sedimentary basins, such as the Lunpola, Nima, and Gaize basins (Figure 1),[8−12] which are oriented W-E and share similar characteristics. These basins are key areas for studying the tectonic uplift and paleotopographic changes in the central Tibetan Plateau. The sedimentary basins in the middle and eastern parts of the BNSZ have amassed a wealth of research achievements.[8,13,14] This study will focus on the Gaize Basin in the western part of the suture zone,[15−17] with an in-depth investigation into its exhumation history and the evolution of its paleotopography. Paleoelevation studies indicate that as early as the Eocene, the altitudes of central Qiangtang, the Tanggula Mountains, and the central Lhasa terrane were all >4 km,[8,18,19] the terrain of hinterland basins has low relief, and the lowlands within the BNSZ were <2.5 km in elevation prior to the Oligocene-Miocene.[10,20,21] Therefore, prior to the Miocene, the central Tibetan Plateau, along the BNSZ, may have already developed a high-altitude, low-relief topography.[1,3,11,22,23] Based on paleoelevation estimates derived from plant fossils,[20] magnetostratigraphy,[10] isotopic dating, and cluster isotope studies,[8] a low-elevation "Central Tibetan Valley" was found to have existed along the BNSZ in the early Cenozoic, which was an east−west trending lowland paleo-valley separated the Gangdese Mountains in the south from the Tanggula Mountains in the north and gradually uplifted and disappeared between 38 and 29 Ma.[8,18,24] Delineating the exhumation history of the Gaize Basin and analyzing the evolutionary process of the paleotopography constitute the focal points in the study of the formation and evolution of the plateau's topography and geomorphology.[10,18,25]

Hu et al.[19] quantitatively traced the paleoelevation changes of the Tibetan Plateau since the Cretaceous by investigating

Received: November 8, 2024
Revised: April 22, 2025
Accepted: May 9, 2025
Published: May 23, 2025

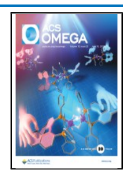

https://doi.org/10.1021/acsomega.4c10175
ACS Omega 2025, 10, 22562−22575

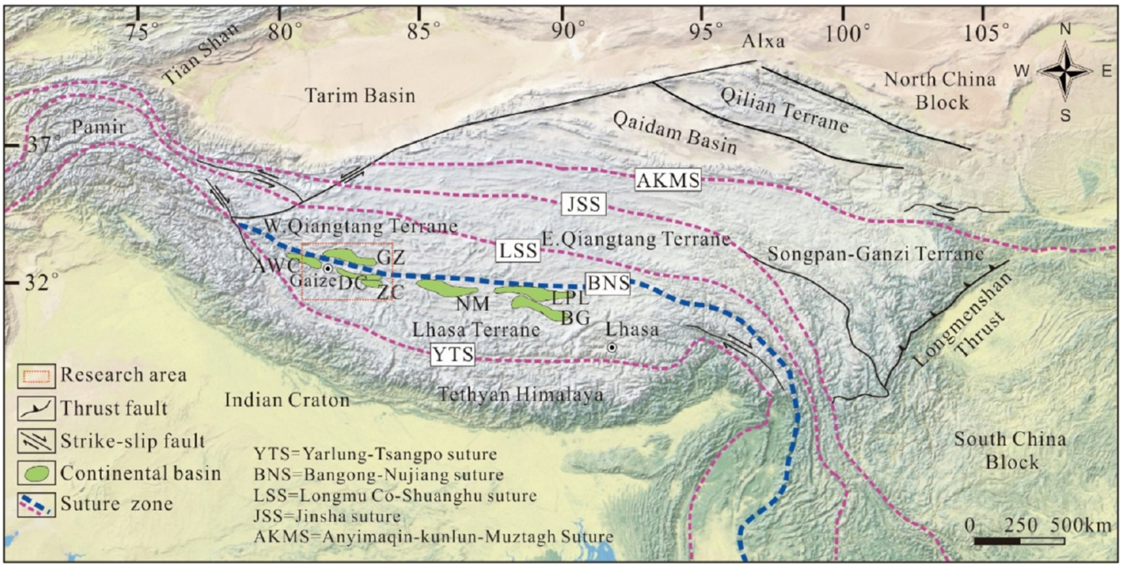

Figure 1. Sedimentary basin complexes within the Bangong-Nujiang Suture Zone (modified from refs 26,27). LPL: Lunpola Basin; BG: Bange Basin; NM: Nima Basin; ZC: Zhongcang Basin; GZ: Gaize Basin; DC: Dongco Basin; AWC: Awongco Basin.

whole-rock Sr/Y and La/Yb ratios. The research findings suggest that there exist regional differences and a multistage uplift process in the uplift of the Tibetan Plateau. Similarly, Tang et al.[28] proposed a novel crustal thickness proxy index based on the Eu anomaly in zircon and reconstructed the evolution of the crustal thickness in Tibet. However, Yakymchuk et al.[29] and Hu et al.[30] indicated that the zircon REE systematic is more complex than previously thought. Low-temperature thermochronology, such as AHe and ZHe, is commonly employed to investigate the cooling and exhumation histories of rock masses. It serves to distinguish the cooling stages of thermal modeling evolution and analyze the exhumation history and long-term evolutionary process of the Gaize Basin during the Late Cretaceous to Paleogene. Constraining the stratigraphic age often relies on the weighted average age of the youngest detrital zircons in zircon U−Pb, which is generally regarded as reliable evidence. The isostatic model of sedimentary accumulation can typically utilize data such as field measurements and seismic profiles to estimate the contribution of sedimentary filling to crustal thickening, specifically the cumulative uplift resulting from the sedimentary isostatic effect.[31] Consequently, we rebuilt the exhumation history of the research area dating back to the Late Cretaceous-Paleogene period and associated the exhumation phases with topographic fluctuations. This provides an effective method for determining the differences in the uplift and growth patterns of the Tibetan Plateau.

The Gaize Basin, located within the BNSZ, is controlled by faults and contains thick sedimentary layers. Based on the current research in this region, a model of its Late Cretaceous-Paleogene evolution was constructed by using zircon U−Pb dating, low-temperature thermochronology, and the isostatic model of the crust; according to the results of the thermal simulation, two cooling−exhumation stages were identified, with multiple tectonic collisions and extrusions; the low-temperature thermochronology study indicates that the 2 phases of cooling events experienced in the Gaize Basin had different tectonically driven mechanisms; using the isostatic model for sedimentary accumulation, the contribution of Paleogene sedimentation effects of the uplift of the land surface was calculated. This research has significant scientific value in revealing the sedimentary infill process, paleotopographic evolution, and uplift history of Cenozoic basins in central Tibet.[6]

2. GEOLOGICAL SETTING

The BNSZ, located in the central Tibetan Plateau, is adjacent to the Qiangtang terrane in the north and connects to the Lhasa terrane in the south. It originates from Bangong Lake in the west, passes through Gaize and Nima in the eastward direction, and then extends southward toward Southeast Asia.[2,4,32] The Gaize Basin, situated within this suture zone, represents one of the crucial regions for the study of tectonic evolution and geomorphic development of the Tibetan Plateau. The formation and evolution of the Tibetan Plateau are primarily driven by the continuous collision and subduction of the India-Eurasia plate. Approximately 50 Ma ago, the northward subduction of the Indian Plate and its collision with the Eurasian Plate triggered the surface uplift of the Tibetan Plateau.[5,33] During the period from the Late Cretaceous-Paleogene, the collision between the Qiangtang-Lhasa terranes and the subduction process of the Neo-Tethys Ocean initiated the primary crustal thickening and shortening within the Tibetan Plateau region.[34,35] In the Paleogene, as the Indian Plate continued its northward subduction, the collision intensified, further driving the uplift of the plateau. This phase was accompanied by the upwelling of asthenospheric magma and activation of thrust faults, resulting in additional crustal thickening and ongoing surface uplift.[16,33] As the Tibetan Plateau continued to rise, the sediments in the Gaize Basin underwent prolonged erosion, gradually being exposed at the surface. The paleotopographic changes during the Late Cretaceous-Paleogene within the basin have unveiled the intricate interrelationships between crustal thickening and denudation, which have provided significant geological evidence for the formation of the high-altitude, low-relief terrain in the Tibetan Plateau region.

The Gaize Basin is positioned within the middlewestern section of the BNSZ, sandwiched between the Lhasa terrane and the Qiangtang terrane. To its east lies the Nima Basin, and

https://doi.org/10.1021/acsomega.4c10175
ACS Omega 2025, 10, 22562−22575

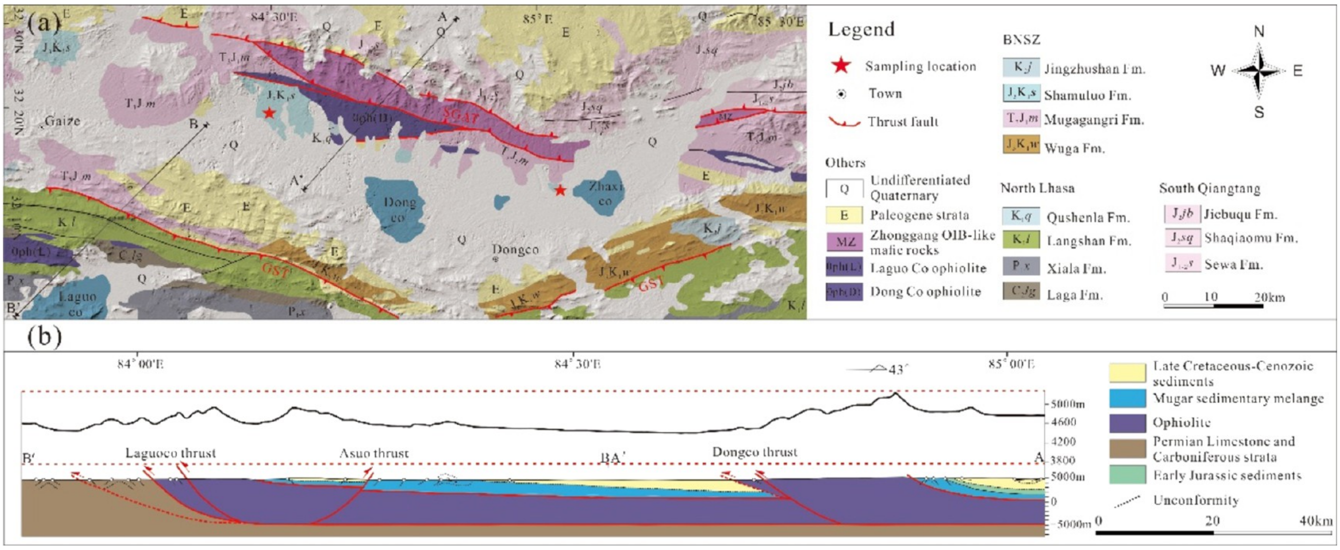

Figure 2. (a) Geological map of the Gaize Basin. (b) Structural cross section and topographic profile of the Gaize Basin (modified from refs 16,39).

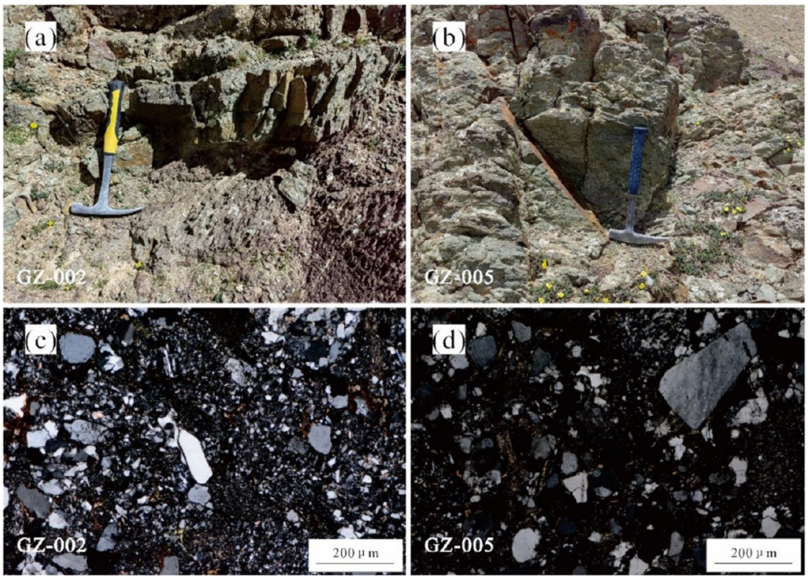

Figure 3. Lithological characteristics of the Shamulou Formation sandstones from the Upper Jurassic-Lower Cretaceous in the Gaize Basin. (a, b) Sampling locations of samples GZ-002 and GZ-005. (c, d) Orthogonal polarization images of thin slices of samples GZ-002 and GZ-005.

to its west lies the Awongco Basin. Since the Late Cretaceous, it has been subjected to intense extrusion and tectonic deformation, and several thrust fault systems have formed;[11,34,36] the Gaize-Selin Co thrust separates the southern basin from the Lhasa terrane, and the Mugagangri thrust within the Shiquanhe-Gaize-Amdo thrust system is the northern boundary of the basin (Figure 2a).[37] To the north, the South Qiangtang terrane displays reverse thrust structures, with Jurassic mélange rocks thrust from N to S above the Paleogene, trending E-S; in the southern part of the basin, Jurassic marine limestone, clastic rocks, and mélange rocks are thrust from S to N above the Paleogene in the basin, also trending E-S (Figure 2b).[34,37,38]

The Gaize Basin is underlain by the Triassic-Jurassic, with outcrops of the Cretaceous Abushan Formation (K_2a) and Qushenla Formation (K_1q), and the Paleogene Nadingco Formation (E*n*), Meisu Formation (E*m*), Kangtuo Formation (E*k*), and Quaternary Formation (Q).[38,40,41] The stratigraphic subdivision of the South Qiangtang include the Riganpeico Formation (T_3r), Sewa Formation ($J_{1-2}s$), Kangtuo Formation (E*k*), and Suonahu Formation (E_2s); and the stratigraphic subdivision of the BNSZ include the Mugagangri Group (J*m*) and the Shamuluo Formation (J_3K_1s). The Shamuluo Formation (J_3K_1s) is a fossil-rich, unmetamorphosed shallow marine carbonate and clastic sedimentary formation; the Mugagangri Group, distributed along the BNSZ, is a Jurassic mélange dominated by gray-black muddy slate and metamorphic sandstone, with interbedded siltstone, limestone, and siliceous limestone.[35,39] The Lower Cretaceous Qushenla Formation (K_1q) andesite is formed along the south side of the thrust fault. The Eocene Nadingco Formation, which is formed in the eastern portion of the basin, unconformably overlies the Kangtuo Formation; the lower portion of the Kangtuo Formation is characterized by purple-red coarse-fine-grained conglomerates interbedded with purple-red and black sandstones, while the upper portion is composed of purple-red

https://doi.org/10.1021/acsomega.4c10175
ACS Omega 2025, 10, 22562−22575

Table 1. Results of Zircon U−Pb Analysis

						age (Ma)				used age (Ma)	
spot no.	Th (ppm)	U (ppm)	Th/U	$^{207}Pb/^{206}Pb$	1σ	$^{207}Pb/^{235}U$	1σ	$^{206}Pb/^{238}U$	1σ	Age	1σ
D604-N-1	122.71	132.28	0.93	322	33	173	3	161	1	161	1
D604-N-2	561.82	442.69	1.27	1828	20	311	4	148	2	148	2
D604-N-3	93.96	61.01	1.54	1877	7	1844	9	1814	14	1877	7
D604-N-4	36.58	35.23	1.04	2528	5	2509	10	2488	22	2528	5
D604-N-5	362.72	202.15	1.79	346	18	315	3	311	2	311	2
D604-N-6	911.84	478.11	1.91	354	11	251	2	240	2	240	2
D604-N-7	172.4	745.66	0.23	272	7	223	2	219	1	219	1
D604-N-8	578.94	540.97	1.07	443	11	265	2	245	2	245	2
D604-N-9	320.14	189.55	1.69	787	3	736	4	720	4	720	4
D604-N-10	198.58	112.71	1.76	350	28	230	3	219	2	219	2
D604-N-11	134.08	111.28	1.2	383	21	293	3	281	2	281	2
D604-N-12	75.96	40.16	1.89	854	19	796	6	774	6	774	6
D604-N-13	75.23	48.37	1.56	2488	5	2409	6	2316	13	2488	5
D604-N-14	63.74	37.54	1.7	328	69	248	7	239	3	239	3
D604-N-15	138.84	202.98	0.68	302	15	258	2	253	2	253	2
D604-N-16	401.05	440.17	0.91	539	7	418	2	397	2	397	2
D604-N-17	87.7	85.18	1.03	2514	3	2428	6	2327	13	2514	3
D604-N-18	76.38	76.31	1	1480	7	1433	5	1403	7	1480	7
D604-N-19	30.64	175.79	0.17	1954	4	1811	7	1690	12	1954	4
D604-N-20	72.27	86.07	0.84	794	34	268	4	211	3	211	3
D604-N-21	118.11	103.96	1.14	300	−6	188	2	180	2	180	2
D604-N-22	106.32	80.49	1.32	320	42	247	5	238	2	238	2
D604-N-23	148.55	81.68	1.82	680	−17	575	4	549	4	549	4
D604-N-24	256.36	645.07	0.4	256	50	179	2	174	1	174	1
D604-N-25	260.04	243.33	1.07	345	17	232	2	221	2	221	2
D604-N-26	192.46	145.39	1.32	1877	6	1773	11	1686	17	1877	6
D604-N-27	28.62	36.9	0.78	2521	7	2509	12	2495	25	2521	7
D604-N-28	91.01	331.03	0.27	1454	20	779	22	544	16	544	16
D604-N-29	59.05	63.82	0.93	1976	58	567	8	281	3	281	3
D604-N-30	358.6	391.12	0.92	276	11	234	2	230	2	230	2
D604-N-31	61.73	81.33	0.76	639	17	468	4	435	4	435	4
D604-N-32	180.05	263.25	0.68	1502	6	1446	7	1408	12	1502	6
D604-N-33	49.18	54.17	0.91	2448	6	2249	12	2036	22	2448	6
D604-N-34	87.84	145.8	0.6	309	12	239	2	232	2	232	2
D604-N-35	208.32	628.99	0.33	250	9	230	2	228	2	228	2
D604-N-36	95.1	119.73	0.79	346	37	239	4	228	2	228	2
D604-N-37	100.11	109.29	0.92	550	36	288	5	256	3	256	3
D604-N-38	40.42	92.7	0.44	1877	6	1760	10	1663	17	1877	6
D604-N-39	94.51	92.95	1.02	1028	13	941	6	904	6	904	6
D604-N-40	36.12	33.56	1.08	609	23	532	7	515	5	515	5
D604-N-41	119.9	99.92	1.2	620	33	393	6	355	2	355	2
D604-N-42	76.37	88.7	0.86	365	35	178	3	165	1	165	1
D604-N-43	0.82	87.6	0.01	569	30	445	5	422	3	422	3
D604-N-44	54.14	37.08	1.46	1633	19	1561	11	1517	14	1633	19
D604-N-45	59.99	30.97	1.94	831	25	775	8	757	8	757	8
D604-N-46	148.24	173.92	0.85	1884	10	1762	8	1659	12	1884	10
D604-N-47	130.99	105.69	1.24	254	28	228	3	225	2	225	2
D604-N-48	68.14	31.55	2.16	2215	6	2156	8	2094	15	2215	6
D604-N-49	23.48	8.43	2.79	1856	15	1841	25	1835	46	1856	15
D604-N-50	12.76	143.7	0.09	1536	4	1531	7	1529	12	1536	4
D604-N-51	25.02	10.68	2.34	609	76	500	15	470	13	470	13
D604-N-52	32.14	94.79	0.34	1869	5	1829	9	1793	16	1869	5
D604-N-53	11.89	6.98	1.7	2466	14	2411	39	2340	84	2466	14
D604-N-54	30.86	64.33	0.48	480	22	446	7	438	7	438	7
D604-N-55	42.95	54.08	0.79	569	50	194	4	166	3	166	3
D604-N-56	88.9	64.59	1.38	1873	7	1840	9	1812	16	1873	7
D604-N-57	143.81	97.62	1.47	989	10	936	9	918	12	918	12
D604-N-58	41.5	67.81	0.61	369	48	295	6	286	4	286	4
D604-N-59	28.19	51.86	0.54	1880	7	1870	11	1864	22	1880	7

https://doi.org/10.1021/acsomega.4c10175
ACS Omega 2025, 10, 22562−22575

Table 1. continued

				age (Ma)						used age (Ma)	
spot no.	Th (ppm)	U (ppm)	Th/U	$^{207}Pb/^{206}Pb$	1σ	$^{207}Pb/^{235}U$	1σ	$^{206}Pb/^{238}U$	1σ	Age	1σ
D604-N-60	39.58	86.73	0.46	324	26	304	5	301	4	301	4
D604-N-61	56.54	31.41	1.8	1856	7	1905	10	1961	18	1856	7
D604-N-62	153.21	122.91	1.25	476	13	476	3	477	3	477	3
D604-N-63	62.38	51.69	1.21	524	19	516	4	514	4	514	4
D604-N-64	28.06	41.08	0.68	1900	8	1874	8	1849	13	1900	8
D604-N-65	53.4	54.22	0.98	2487	8	2501	7	2520	17	2487	8
D604-N-66	48.07	23.38	2.06	789	219	741	7	728	7	728	7
D604-N-67	103.34	111.33	0.93	476	19	389	4	374	3	374	3
D604-N-68	32.58	151.34	0.22	976	7	932	5	913	6	913	6
D604-N-69	41.2	56.31	0.73	478	16	428	4	421	3	421	3
D604-N-70	222.21	161.04	1.38	1040	18	373	3	275	2	275	2
D604-N-71	77.74	60.54	1.28	498	24	431	4	419	3	419	3
D604-N-72	80.75	79.99	1.01	389	26	339	4	333	3	333	3
D604-N-73	77.69	214.5	0.36	265	15	239	2	236	1	236	1
D604-N-74	207.54	156.23	1.33	606	32	468	6	440	3	440	3
D604-N-75	54.87	181.59	0.3	206	23	181	2	179	2	179	2
D604-N-76	82.24	129.11	0.64	2521	4	2461	8	2389	17	2521	4
D604-N-77	44.36	134.03	0.33	998	7	925	5	895	7	895	7
D604-N-78	42.61	71.14	0.6	1883	12	1880	10	1877	16	1883	12
D604-N-79	16.51	92.42	0.18	317	47	227	6	217	3	217	3
D604-N-80	50.06	48.29	1.04	2542	8	2469	10	2382	22	2542	8

coarse conglomerates and fine conglomerates interbedded with light gray coarse sandstones and fine sandstones.[15,41,42]

3. SAMPLING AND METHODS

A total of 3 samples from the Shamuluo Formation were collected from the Gaize Basin. One medium-grained feldspar quartz sandstone sample (D604-N) was analyzed for zircon U−Pb chronology; two sandstone samples (GZ-002 and GZ-005) were subjected to AHe and ZHe analysis and thermal evolution simulations, respectively, and the sampling locations are located in the Gaize Basin of the BNSZ (Figure 3). In this study, we acknowledge that the limited sample size may render the research findings not universally applicable. Nevertheless, the current results can still impose constraints on the regional uplift and exhumation history. In subsequent research, we will increase the sample size, expand the sampling scope, and further compare with previous research results to enhance the accuracy of our findings.

3.1. Zircon U−Pb Chronology. The zircon separation and target preparation for sample D604-N were carried out at the Experimental Testing Center of the Hebei Regional Geological Survey Institute. The extraction of zircon crystals was carried out by means of standard crushing and separation techniques. The zircon U−Pb dating was carried out at the Institute of Mineral Resources under the Chinese Academy of Geological Sciences, with the employment of the LA-ICP-MS analytical technique. The analysis was conducted with an Agilent 7700x laser ablation inductively coupled plasma mass spectrometer that was paired with a 193 nm laser ablation system. Zircon 91500 served as the external standard for isotope fractionation correction, possessing an average age of 1062 ± 8 Ma, which was congruent with the conventionally recognized age.[43] The Concordia diagram and Kernel Density Estimation (KDE) diagram were generated using IsoplotR software.[44,45] Offline data analysis was conducted using ICP-MS Data Cal software, with detailed instrument operating conditions and data processing methods as outlined in Liu et al.[43,45] (Table 1).

3.2. Apatite and Zircon (U−Th)/He and Thermal Evolution Simulations. AHe and ZHe datings are commonly used for low-temperature thermochronological dating and thermal history simulation and can reveal the driving mechanism of the exhumation process and rapid cooling.[46] In order to explore the correlation among thrust faulting, uplift exhumation, fluvial transport, and the sedimentary record, two samples of Shamuluo Formation sandstones were obtained from the lower plate of the Dongcuo thrust fault (Figure 2a).

Samples GZ-002 and GZ-005 were completed in the laboratory of the Hebei Provincial Geological Survey Institute and the National Institute of Natural Disaster Prevention and Control. The sandstone samples to be tested were crushed to 80−100 mesh powder, drained, and sieved; the selected apatite and zircon particles were wrapped in sulfate paper and set aside. Follow-up experiments were carried out following the procedure of Foeken[47] et al: apatite and zircon grains with intact grain shape, without internal inclusions, and a minimum width of 65 μm or more were selected,[48,49] and the ^{4}He content of the grains was measured with an Alphachron He isotope mass spectrometer. The apatite and zircon particles underwent a two-step heating process by using a 970 nm diode laser. Subsequently, the extracted ^{4}He was diluted with ^{3}He. For the isotopic analyses, a quadruple rod mass spectrometer was utilized. Prior to this, samples were purified with a SAES AP10N zirconium−aluminum pump for 5 min to eliminate reactive gases.

After the ^{4}He content determination is completed, the sample grains will be transferred to a solution bottle, 7 mol/L of HNO_3 and 25 μL of U and Th diluent will be added, the dissolution bottle will be left at room temperature for 4 h (10 h for zircon), and MiniQ ultrapure water will be added to the dissolution bottle. Diluted standard and sample solutions were completed on an Agilent 7900 ICP-MS, yielding AHe and ZHe

https://doi.org/10.1021/acsomega.4c10175
ACS Omega 2025, 10, 22562−22575

Table 2. Results of Apatite (U−Th)/He Analysis

spot no.	Th (ppm)	U (ppm)	Th/U	[EU]	length (μm)	width (μm)	Rs	FT	initial age age ± σ(Ma)	corrected age age ± σ(Ma)
GZ-002−1A	4.64	30.11	6.71	11.71	212.20	105.00	62.88	0.69	35.05 ± 0.64	50.71 ± 0.93
GZ-002−2A	1.79	13.13	7.58	4.88	199.33	119.06	69.05	0.72	40.91 ± 0.84	57.00 ± 1.17
GZ-002−3A	0.15	2.60	18.01	0.76	187.92	124.37	69.92	0.72	62.47 ± 1.76	87.32 ± 2.46
average age (Ma)									39.15 ± 3.56	55.87 ± 6.78
GZ-005−1A	2.42	22.83	9.74	7.79	161.77	116.30	64.86	0.70	36.8 ± 0.70	52.76 ± 1.00
GZ-005−2A	2.74	27.01	10.19	9.09	314.59	219.76	130.84	0.85	36.88 ± 0.73	43.40 ± 0.86
GZ-005−3A	3.59	28.99	8.34	10.41	196.09	121.60	63.84	0.69	38.35 ± 0.77	55.27 ± 1.11
average age (Ma)									37.29 ± 0.29	49.39 ± 2.97

Table 3. Results of Zircon (U−Th)/He Analysis

spot no.	Th (ppm)	U (ppm)	Th/U	[EU]	length (μm)	width (μm)	Rs	FT	initial age age ± σ(Ma)	corrected age age ± σ(Ma)
GZ-002−1Z	64.98	17.43	0.28	69.07	192.44	100.90	59.50	0.79	48.82 ± 1.31	61.83 ± 1.66
GZ-002−2Z	345.44	54.07	0.16	358.14	116.20	72.46	40.98	0.70	60.95 ± 1.67	86.46 ± 2.37
GZ-002−3Z	242.79	49.50	0.21	254.42	156.66	71.56	44.41	0.72	57.84 ± 1.56	79.79 ± 2.15
average age (Ma)									54.78 ± 4.57	72.75 ± 12.35
GZ-005−1Z	154.37	70.34	0.47	170.90	187.91	83.72	48.41	0.74	74.42 ± 1.92	100.38 ± 2.59
GZ-005−2Z	231.08	77.71	0.35	249.34	183.78	104.28	59.46	0.79	62.83 ± 1.67	79.70 ± 2.12
GZ-005−3Z	396.79	129.60	0.34	427.24	167.98	88.10	51.86	0.76	62.87 ± 1.67	82.78 ± 2.20
average age (Ma)									66.03 ± 5.19	86.13 ± 11.17

ages, weighted average ages of the samples, and isotopic contents of individual grains (Tables 2 and 3). Thermal history inversion simulations were performed using HeFTy software with the following constraints: (1) The U−Pb age of the antecedent detrital zircon was employed to constrain the age of the sedimentary stratigraphy within the region.[50−52] (2) The temperature at the onset of the stratigraphy's initial deposition averaged around (10 ± 5) °C. (3) The average temperature at the surface of the present-day Gaize Basin is 10 ± 5 °C. (4) The confinement temperatures of the apatite samples are 40−70 °C, and the closure temperature of zircon samples is 130−200 °C. The thermal history simulations derived using the HeFTy software were simulated as "Good" when the GOF value was greater than 0.5 and were considered "Acceptable" when the GOF value was only greater than 0.05. For the simulation results not to exclude more possibilities within the error range because of the constraints, a time interval slightly larger than the particle age range of the sample was selected as a constraint.

3.3. Isostatic Model of the Crust. In the context of endorheic basins, the processes of crustal shortening and sediment accumulation are capable of inducing surface uplift. The basement of the sedimentary zone within the BNSZ is relatively rigid with limited crustal shortening, while sediment accumulation contributes to the uplift of the Gaize Basin. According to the isostatic model (Figure 4), the amount of surface uplift caused by sediment accumulation can be calculated by measuring the thickness of the Paleogene sediments within the basin.[31,53]

Due to compaction, the density of the sediment increases with depth, and assuming an exponential decreasing trend in the porosity of the sediment,[54,55] the density of the sediment can be expressed as follows[53]

$$\rho_b(h) = \rho_0\text{-}(\rho_0\text{-}\rho_s)e^{-ch} \tag{1}$$

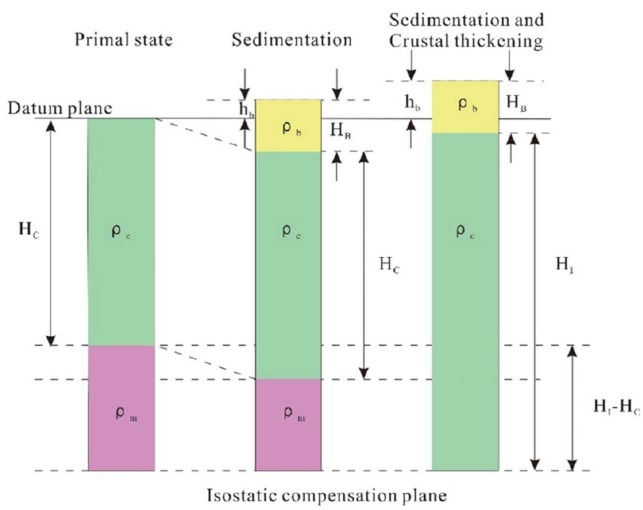

Figure 4. Isostatic model of sedimentary basins (modified from refs31,53): H_B is the total sediment thickness; H_C is the initial crustal thickness before tectonic shortening; H_I is the crustal thickness after tectonic shortening; h_b is the surface uplift caused by sedimentary strata; ρ_m is the mantle density; ρ_c is the crustal density; and ρ_b is the density of the sediments.

The condition for equalization compensation can be expressed as follows[53]

$$\int_0^{h_b} \rho_b(h)dh = \int_{h_b}^{H_B} [\rho_m - \rho_b(h)]dh \tag{2}$$

The derivation of eq 2 yields eq 3, which is the formula for the augmentation amplitude (h_b) due to sedimentation[31,53]

$$h_b = \frac{\rho_m - \rho_0}{\rho_m}H_B - \frac{\rho_0 - \rho_S}{c\rho_m}(e^{-cH_B} - 1) \tag{3}$$

https://doi.org/10.1021/acsomega.4c10175
ACS Omega 2025, 10, 22562−22575

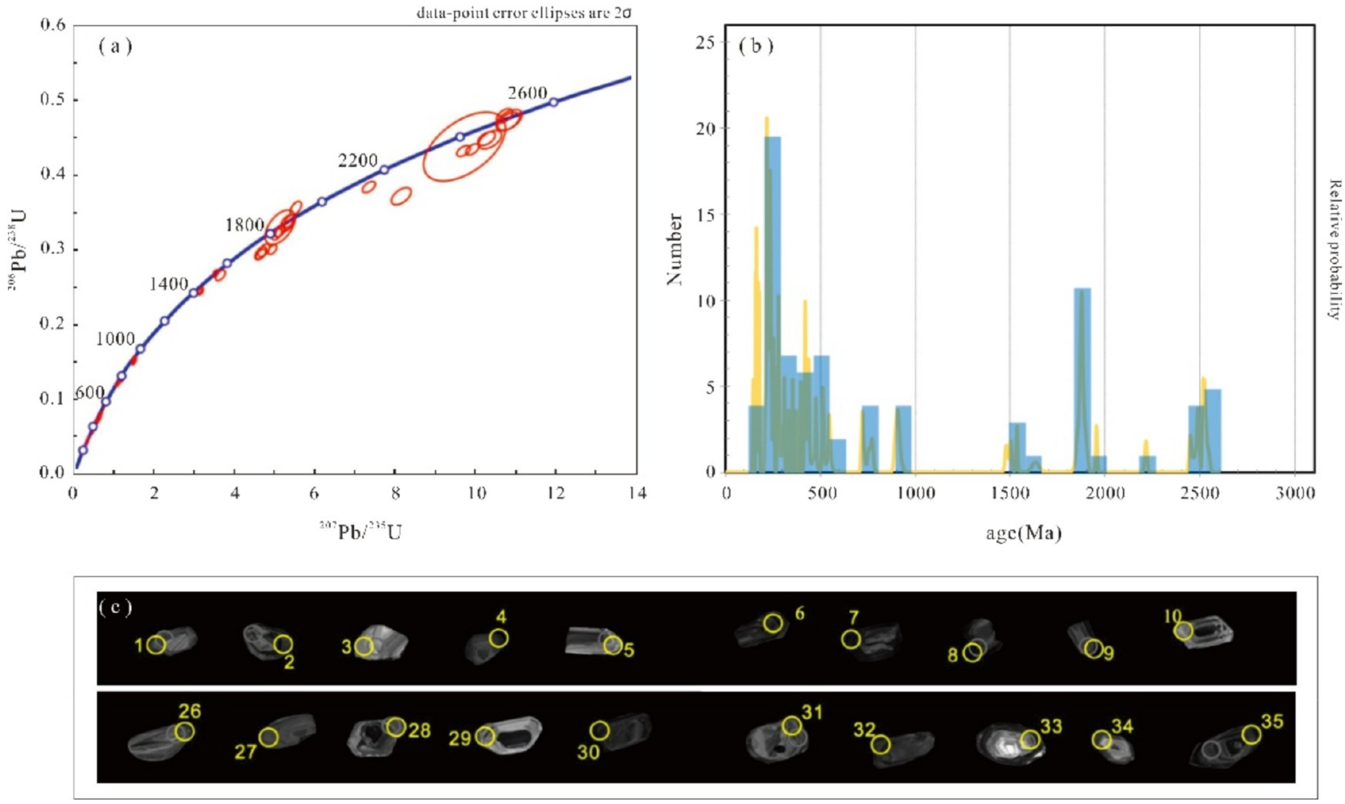

Figure 5. (a) Concordia diagram showing the results of zircon U−Pb analyses (ages in Ma). (b) KDE of detrital zircon from the Shamuluo Formation in the Gaize Basin. (c) Representative CL images of detrital zircons.

The degree of sediment compaction varies with depth, so sediment thickness (H_P) needs to be corrected in paleo-elevation estimation.[31,53]

$$\int_0^{H_P} \rho_b(h)dh = \int_{H_B-H_M}^{H_B} \rho_b(h)dh \tag{4}$$

Eq 5 is derived from eq 4

$$\rho_0 H_P + \frac{1}{c}(\rho_0 - \rho_s)(e^{-cH_P} - 1) = \rho_0 H_M + \frac{1}{c}(\rho_0 - \rho_s)(e^{-cH_B} - e^{-c(H_B - H_M)}) \tag{5}$$

The corrected deposition thickness H_P can be calculated from eq 5.

H_B is the total sediment thickness; H_M is the modern observed sediment thickness of the target layer; H_P is the corrected sediment thickness; and h_b is the surface uplift induced by the sedimentary strata. The mantle density (ρ_m) is taken to be 3.3 × 10^3 kg/m^3; the particle density (ρ_0) to be 2.7 × 10^3 kg/m^3; and the surface sediment density (ρ_s (h = 0)) to be 2.2 × 10^3 kg/m^3 and the constant c was taken as 4 × 10^{-4} m^{-1}.[55]

4. ANALYTICAL RESULTS

4.1. Zircon U−Pb Dating Results. U−Pb dating of detrital zircons from sample D604 of the Shamulou Formation in the Gaize Basin was conducted, yielding 80 data points. The analysis using the Discordance Index showed that no zircon age exceeded 10% discordance, indicating that the ages of all 80 data points are stable. These results suggest that the zircons have not undergone significant thermal alteration or metamorphism, providing a reliable geological age estimate. The ages reflect the sample's original formation time and stability, with no apparent influence from later geological events (Figure 5a). The youngest zircon ^{206}Pb/^{238}U age measured in the sample is 161 ± 1 Ma, indicating that the Shamuluo Formation was not deposited earlier than the Late Jurassic (Table 1). Li et al. stated that the youngest detrital zircon within the Shamuluo Formation was dated at 113 Ma, suggesting that the sedimentary process of the Shamuluo Formation potentially persisted from the Late Jurassic to the late Early Cretaceous.[50−52]

Sample D604-N zircon ages show 256−217 and 1954−1856 Ma as the most prominent age peaks, along with 550−470, 440−397, 918−720, and 2542−2448 Ma age peaks (Figure 5b). The ^{206}Pb/^{238}U age ranges from 256 to 217 Ma, with 16 age points, 12 of which have zircon Th/U values >0.4, and 4 have zircon Th/U values between 0.1 and 0.4. In the second group, there are 12 sites with ^{207}Pb/^{206}Pb ages between 1954 and 1856 Ma (Figure 5b), and all of them have Th/U values >0.1. In zircon U−Pb geochronology, the ^{207}Pb/^{206}Pb ratio exhibits relatively lower susceptibility to error in older samples, demonstrating a reduced impact from lead loss and consequently providing more stable and reliable age determinations. In the CL images, the majority of the aforementioned zircons display magmatic oscillatory zones, indicative of their nature as magmatic zircons (Figure 5c).

4.2. (U−Th)/He Experimental Results. When selecting different mineral particles from individual rock samples, particles with relatively similar grain sizes were chosen, and there was no significant positive correlation between the spherical equivalent radius and the initial age of (U−Th)/He for all of the mineral particles tested; the initial age of (U−

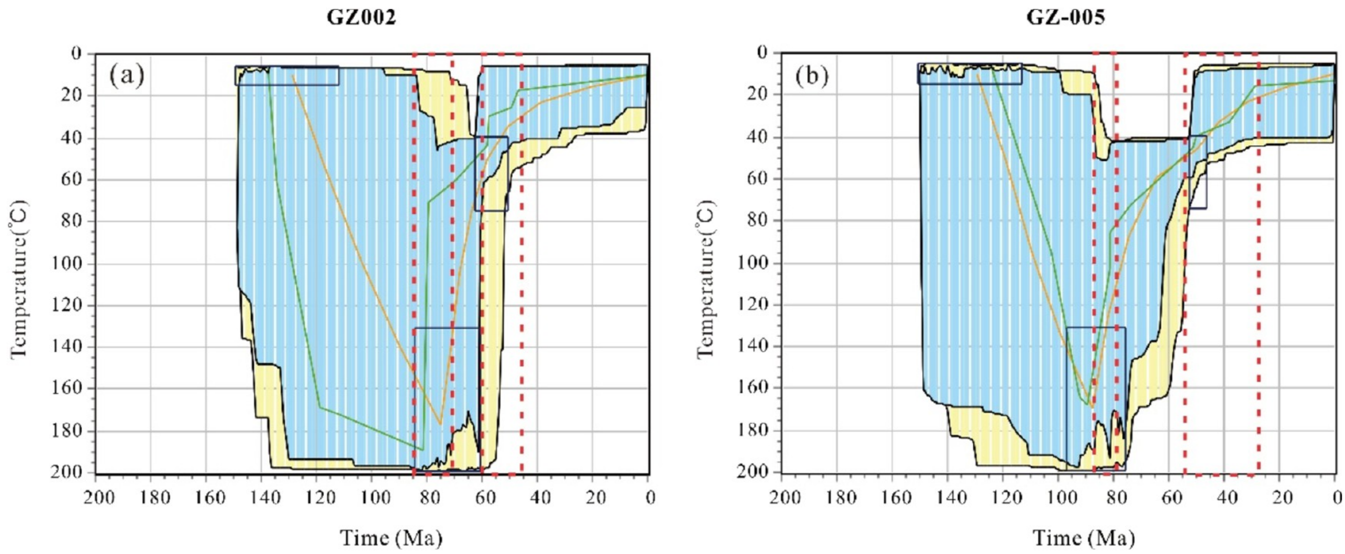

Figure 6. Simulation results of thermal evolution in the Gaize Basin. The blue boxes are time−temperature bounding boxes. "Good" results (fit >0.55) are represented by the blue area. "Acceptable" results (fit > 0.05) are represented by the yellow area. The orange thick line represents the weighted average of all results. The green thick line represents the best-fit curve. The red dashed box represents a cooling onset or cooling acceleration event.

Th)/He and the effective uranium concentration for apatite and zircon particles did not show any significant positive correlation, and the mineral particles were less affected by the radiation damage. The AHe and Zhe corrected ages do not show a significant negative correlation with the effective uranium concentration, and the experimental data have been Ft-corrected, suggesting that the age values obtained from the tests are less affected by zircon and apatite (α-particles) injections and ejections.[56]

The α-particle damage-corrected AHe single-grain weighted average age of sample GZ-002 is 55.87 ± 6.78 Ma, and the ZHe single-grain weighted average age is 72.75 ± 12.35 Ma. The α-particle damage-corrected AHe single-grain weighted average age of sample GZ-005 is 49.39 ± 2.97 Ma, and the ZHe single-grain weighted average age is 86.13 ± 11.17 Ma. The single-grain weighted mean ages of AHe and ZHe for both samples are less than the depositional age (Tables 2, 3). This age proves to be the time limit for the most recent thermal−historical evolution of the sedimentary strata, as recorded by the complete annealing of the mineral grains after deposition.

The three AHe single-grain ages and errors of GZ-002 are 50.71 ± 0.93, 57.00 ± 1.17, and 87.32 ± 2.46 Ma, respectively, of which the two younger ages are similar, and 87.32 ± 2.46 Ma is close to the stratigraphic depositional age. The corrected AHe weighted average age of GZ-002, 55.87 ± 6.78 Ma, is more consistent with the actual thermal history evolution process, so the time limit range of 63−50 Ma was selected.

The ages and errors of the three AHe single particles of GZ-005 are 52.76 ± 1.00, 43.40 ± 0.86, and 55.27 ± 1.11 Ma, respectively, which are similar to the younger ages of the two AHe of sample GZ-002, and the sampling distances of GZ-002 and GZ-005 are closer together and combined with the tectonic evolutionary process of the Gaize Basin. The weighted average age and error of the three AHe single grains in sample GZ-005 is 49.39 ± 2.97 Ma, and the time-limited range of AHe is 53−47 Ma (Table 3).

The three ZHe single-particle ages of GZ-002 and their errors are 61.83 ± 1.66, 86.46 ± 2.37, and 79.79 ± 2.15 Ma, of which 79.79 ± 2.15 Ma is extremely similar to the single-particle age of 79.70 ± 2.12 Ma of sample GZ-005, and the combination of the corrected weighted age and the error of 72.75 ± 12.35 Ma, GZ-002 has a time-limited range of 85−60 Ma in ZHe, which allows for thermal history inversion simulations.

The three ZHe single-grain ages of GZ-005 and their errors are 100.38 ± 2.59, 79.70 ± 2.12, and 82.78 ± 2.20 Ma, respectively, of which 100.38 ± 2.59 Ma is close to the stratigraphic depositional age. Combined with the corrected weighted age and error of 86.13 ± 11.17 Ma, a time limit range of 97−75 Ma for the ZHe was selected.

4.3. Thermal Evolution Simulation Results. Substituting the above experimental results into the HeFTy software simulation, sample GZ-002 experienced a rapid cooling event during 85−70 Ma, with an extremely rapid temperature drop, and it is hypothesized that the collision of the Lhasa and Qiangtang terranes led to the overall uplift of the Gaize Basin and the sharp acceleration of the exhumation; then, two rapid cooling events of a smaller scale occurred again during the period of 60−45 Ma (Figure 6a).

Sample GZ-005 underwent a rapid cooling event during 87−78 Ma, followed by a longer period of burial, and then two smaller-scale rapid cooling events occurred again during 54−26 Ma (Figure 6b). In conclusion, the Late Cretaceous-Paleogene Gaize Basin is divided into two cooling events, 87−70 and 56−26 Ma.

4.4. Calculation of the Isostatic Model. Based on the sedimentary stratigraphic data of the Zhongcang (ZC) profile of the Paleogene Suonahu Formation[15] and the Mengdangle (MDL) profile of the Kangtuo Formation[15,57] in the Gaize Basin, and based on the empirical formula of the isostatic model, the actual contribution of the Paleogene depositional action to the surface uplift can be calculated. Among them, the MDL profile is divided into 131 layers, visible at the top and bottom of the profile, with a total thickness of about 1100 m (Figure 7a); the ZC profile is divided into 86 layers, with the top and bottom of the section visible and a total thickness of about 330 m (Figure 7b).

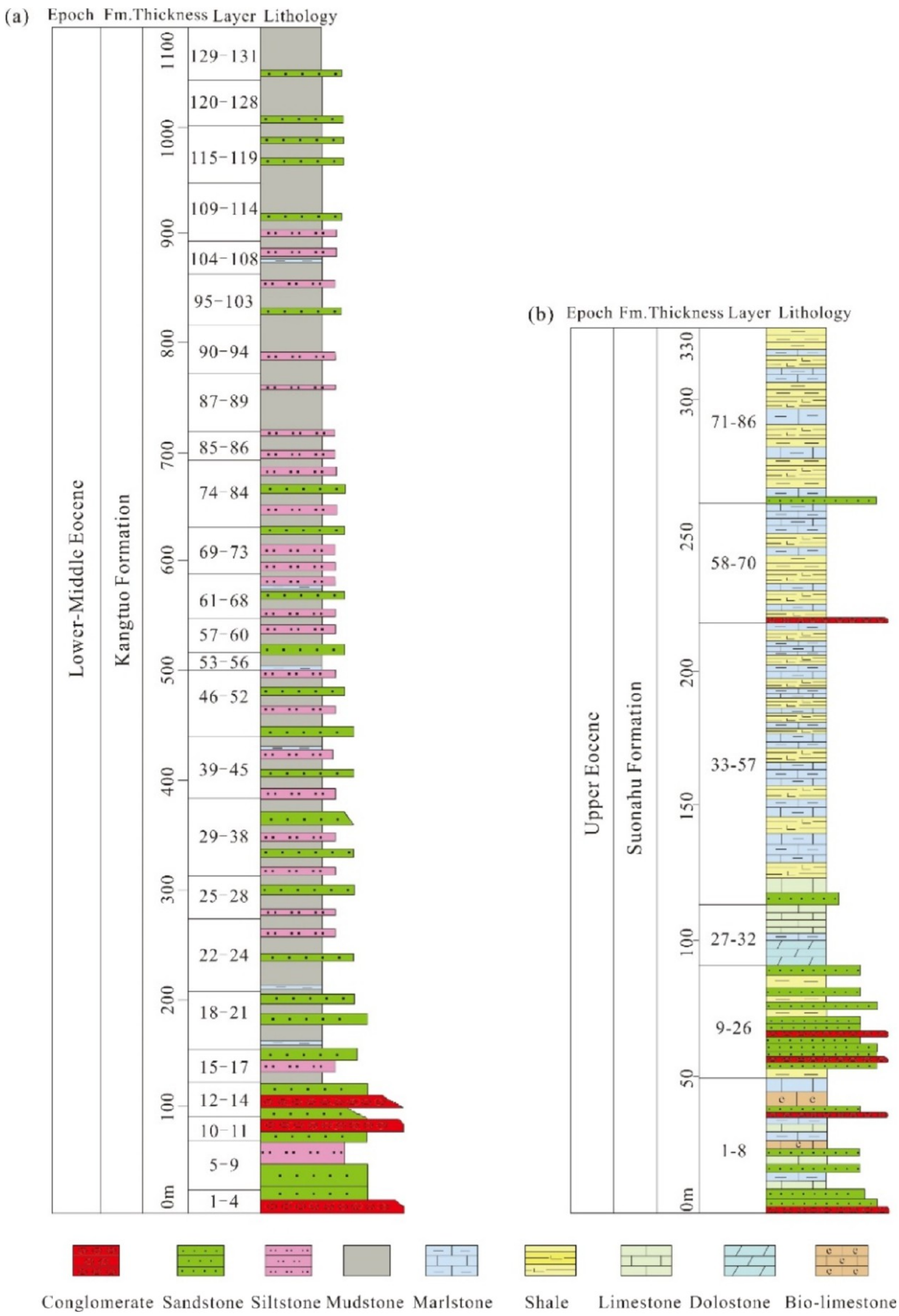

Figure 7. Stratigraphic column diagrams of the MDL profile and ZC profile in the Paleogene of the Gaize Basin (modified from refs 15,57). (a) Lithologic column of Kangtuo Formation in MDL section. (b) Lithologic column of Suonahu Formation in the ZC section.

The BNSZ in the Gaize Basin is considered a rigid basement,[58,59] and the rigid block did not undergo significant crustal shortening uplift, and at this time, the important cause of uplift in the closed Gaize Basin was sediment accumulation.[53,60] Calculated according to the aforementioned formula, the corrected sediment thickness of the Kangtuo Formation is 1400 m and the height of surface uplift caused is 417 m. The corrected sediment thickness of the Suonahu Formation superimposed on the Kangtuo Formation is 1430 m, and the height of surface uplift caused is 425 m. According to the stratigraphic relationship between the Paleogene Kangtuo Formation and the Suonahu Formation,[15] the cumulative contribution of the two to the thickness of the formation is about 0.4 km.

5. DISCUSSION

5.1. Late Cretaceous (87−70 Ma) Exhumation History. In the Late Cretaceous period, the rapid cooling event was due to the collision between the Qiangtang and Lhasa terranes, triggering a surface uplift process. Driven by the subduction of the New Tethys Ocean, the continued compression and accretion following the collision of the

https://doi.org/10.1021/acsomega.4c10175
ACS Omega 2025, 10, 22562−22575

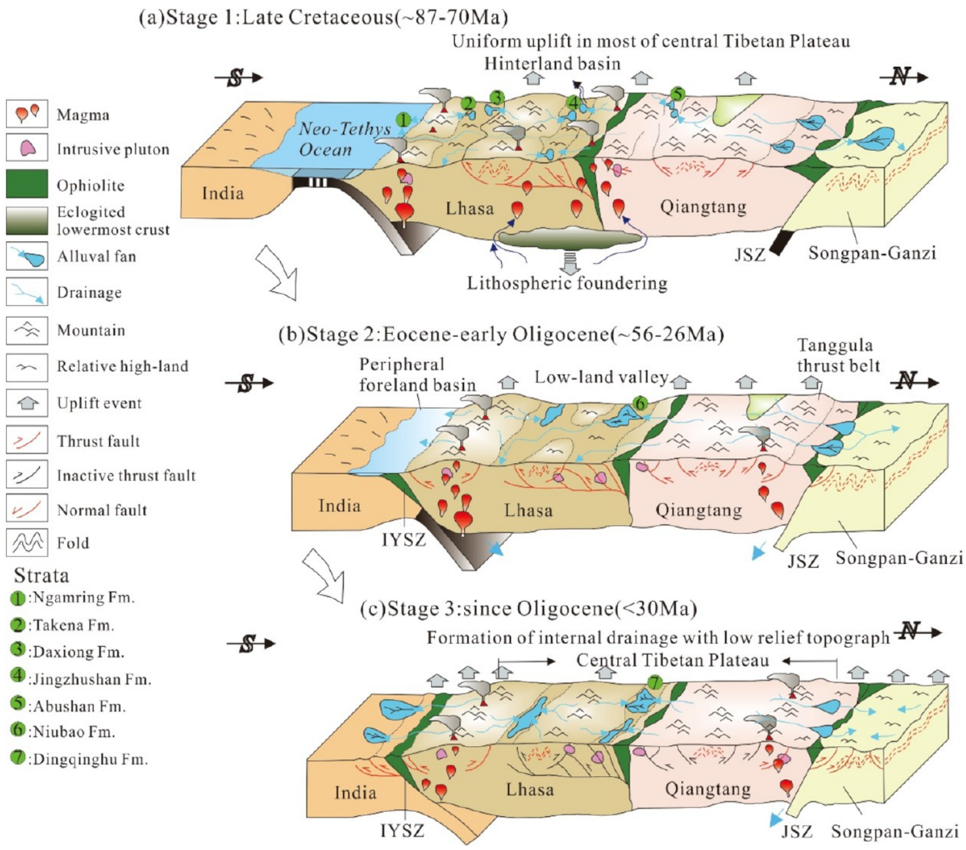

Figure 8. Schematic diagram of the tectonic evolution of the Late Cretaceous-Paleogene in the Central Tibet Valley (modified from ref 35).

Qiangtang and Lhasa terranes not only resulted in crustal shortening and thickening but also led to lithospheric delamination (Figure 8a).[40] This sequence of tectonic activities hastened the plateau's uplift in the Late Cretaceous, which in turn caused a swift decline in surface temperatures and initiated cooling and exhumation occurrences. Particularly between 87 and 70 Ma, the Gaize Basin underwent significant cooling and exhumation, which is highly consistent with previous studies conducted in the northern Lhasa terrane,[23] the eastern segment of the BNSZ Amdo region,[61] and the Qiangtang terrane.[1,23,62−65] These cooling and exhumation phenomena are not only reflected in the exposure of surface sediments but also demonstrate the dynamic evolution of the crust and lithosphere of the Tibetan Plateau. From the Late Early Cretaceous-Paleogene, extensive tectonic shortening in the southern regions of the Qiangtang terrane and the Lhasa terrane further attested to the intense crustal compression that the plateau endured during this period. This compression, in turn, spurred the rapid uplift of the surface.[34,65,66] Moreover, the occurrence of K-rich adakites and Mg-rich magmatic activity provides crucial evidence of crustal thickening during this period. These magmatic occurrences imply that considerable crustal thickening took place in the central Tibetan Plateau during the Late Cretaceous, followed by lithospheric delamination events that led to rapid surface uplift.[67−72]

5.2. Paleogene (56−26 Ma) Exhumation History. During this stage, the swift cooling and exhumation occurrences within the Gaize Basin reflect the complexity of crustal dynamics throughout the India-Asia collision, particularly the ongoing northward subduction of the Indian continent and its interaction with the Asian continent. As this tectonic process continued, the Gaize Basin underwent intense tectonic uplift, magmatic activity, and large-scale compressional deformation (Figure 8b).[40,73−76] Especially during the Paleocene, surface uplift was closely linked to tectonic processes such as magmatic upwelling, lower crust flow,[33,77] and upper crust shortening,[31] which collectively drove the overall uplift of the basin. From the middle Eocene to late Oligocene, the geological environment of the Gaize Basin underwent significant changes. The early-formed thrust fault systems were reactivated, marking a strong response to deep-seated tectonic activities. The activity of the Shiquanhe-Gaize-Amdo thrust fault and the southern Gaize-Selin Co thrust fault signaled that tectonic movements within the basin were still ongoing, and the movements of these faults played a crucial role in shaping the geomorphology and evolution of the Gaize Basin. Accompanying these tectonic processes, surface river erosion gradually intensified, particularly enhanced river transport and erosion, which led to the development of a highly undulating topography in the basin. This process significantly accelerated regional exhumation.[16] Xiong et al.[8] pointed out that during this period, a “Two mountains sandwiching a basin” Central Valley structure emerged, reflecting the contrasting erosion rates of the rock layers inside and outside the basin and the strong influence of tectonic activity.

According to the isostatic model for sedimentary accumulation, the contribution of sediment accumulation caused by Paleogene erosion and fluvial transport to surface uplift significantly increased, with sediment deposition contributing approximately 0.4 km to the surface uplift of the Gaize Basin. The BNSZ, where the Gaize Basin is located, is underlain by a

https://doi.org/10.1021/acsomega.4c10175
ACS Omega 2025, 10, 22562−22575

rigid block with the surrounding mountains rising from the north and south as the exhumation zone. Within the Gaize-Nima-Lunpola basin system adjacent to the BNSZ, the sedimentary strata dating back to the Eocene-Oligocene period typically possess a thickness ranging from 2 to 4 km,[36,78] indicating significant topographic relief in the surrounding areas during sediment deposition. As the external drainage system shifted to an internal drainage system,[79] through river transport, the basin floor began to receive inputs of sediments cut by rivers and transported by erosion, which slowly accumulated, filling the enclosed Gaize Basin. The alterations in the sedimentary environment imply that the central Tibetan Plateau possessed a comparatively prominent topographic relief in the early Cenozoic. From the Eocene-Oligocene, its surface was subjected to both erosional and basin-filling procedures. This contention is further corroborated by the isostatically compensated basin infilling paradigm.[31,60]

The research on the Central Valley has primarily focused on the narrow region to the south of the BNSZ, particularly along the Gaize-Nima-Lunpola basin. During the Eocene-early Oligocene, the Qiangtang terrane underwent extensive exhumation. In light of this, the following interpretation is put forward: this paleo-valley with a relatively low elevation mirrors the altitude of mountain basins that were principally formed within the Lhasa terrane. During the early Eocene and early Oligocene, rapid exhumation and erosion were likely related to the flow patterns of external drainage systems. Water mainly followed the east−west trending lowland river valleys and flowed toward the southeast, carrying with it a substantial quantity of eroded materials from the adjacent mountains. Eventually, these materials were deposited in the marine region at the southern edge of the Lhasa terrane.[12,13]

5.3. Formation of Low-Relief Topography in the Oligocene. Subsequent to the vigorous exhumation incidents during the early Cenozoic, as a result of the incessant collision between the Indian Plate and the Eurasian Plate, the Tibetan Plateau was subject to a process of diminished tectonic deformation and smoothening of the topography, concurrent with its intense uplift. In this phase, crustal uplift and lithospheric shortening occurred simultaneously and the tectonic activity began to stabilize, accompanied by the formation of an arid climate. Consequently, the central region of the Tibetan Plateau gradually evolved into a landform characterized by high-altitude, low-relief terrain. Meanwhile, localized tectonic subsidence and sedimentation contributed to the final shaping of the Central Valley (Figure 8c).[7,23] Since the early Oligocene, the cooling and exhumation rate of the Gaize Basin in the central Tibetan Plateau has been limited, and the erosion rate has gradually slowed. The internal drainage system further developed,[12] and the sedimentation rate decreased, leading to a reduction in topographic differences.[80] The basin gradually filled during the Oligocene and eventually formed a high and wide interior drainage area. By ~30 Ma, the central Tibetan Plateau had already developed a well-defined low-relief topography.[16]

Detrital zircon U−Pb dating results and paleocurrent investigations indicate that the southern border of the Gaize Basin is precipitous, and the sediment sources underwent a remarkable variation during the late Eocene period.[15,81] The Lhasa terrane to the north of the basin provided abundant source material, especially detrital material from this region, which further accelerated the sedimentary filling within the basin. This study additionally revealed that the sediment sources of the Gaize Basin exhibit substantial resemblance to those of the Nima and Lunpola Basins. This similarity lends credence to the supposition that during the early Cenozoic, these basins might have constituted a section of a low-altitude valley among mountains. Overall, the erosion, exhumation, and sedimentary infilling of the basin clusters along the BNSZ were shaped by the reactivation of thrust fault systems, the low-relief topography that resulted, and the river incision. This provided important evidence for further deciphering the region's tectonic evolution history.

The Gaize Basin's low-relief characteristics reflect the landscape adjustment process following the uplift, whereas the Central Valley's gentle topography indicates that its formation was influenced by the development of the internal drainage system and tectonic adjustments following the overall uplift. The formation of this series of geomorphological features not only reflects the overall uplift pattern of the Tibetan Plateau but also provides valuable insights into understanding its geological characteristics and dynamic mechanisms.

6. CONCLUSIONS

(1) The Shamuluo Formation in the Gaize Basin has the youngest detrital zircon U−Pb age of 161 Ma, constraining its deposition age to the Late Jurassic-Early Cretaceous. Using this constraint, thermal history modeling based on AHe and ZHe dating results suggests that the Gaize Basin underwent two episodes of rapid cooling and exhumation, occurring between 87−70 and 56−26 Ma.

(2) The exhumation events during the Late Cretaceous are associated with surface uplift in the central Tibetan Plateau, driven by the ongoing collision of the Qiangtang and Lhasa terranes and the subduction of the New Tethys Ocean. The Paleogene exhumation events correspond to surface uplift caused by the continued collision between the Indian and Eurasian plates and the northward subduction of the Indian plate, with sedimentary accumulation contributing about 0.4 km to the surface uplift. By the early Oligocene, the high-altitude, low-relief topography of the central Tibetan Plateau had become fully established.

■ AUTHOR INFORMATION

Corresponding Author

Wentian Mi − *College of Resource and Environmental Engineering, Inner Mongolia University of Technology, Hohhot 010051, China*; Email: migeochemistry@126.com

Authors

Yuan Gao − *College of Resource and Environmental Engineering, Inner Mongolia University of Technology, Hohhot 010051, China*; orcid.org/0009-0007-3360-6323

Wenguang Yang − *Institute of Sedimentary Geology, Chengdu University of Technology, Chengdu 610059, China*

Guozhong Ji − *Institute of Sedimentary Geology, Chengdu University of Technology, Chengdu 610059, China*

Yuhang Luo − *School of Earth Sciences, Lanzhou University, Lanzhou 730000, China*; orcid.org/0000-0002-8891-0230

https://doi.org/10.1021/acsomega.4c10175
ACS Omega 2025, 10, 22562−22575

Ke Miao − *College of Resource and Environmental Engineering, Inner Mongolia University of Technology, Hohhot 010051, China;* orcid.org/0009-0007-1669-6961

Complete contact information is available at: https://pubs.acs.org/10.1021/acsomega.4c10175

Notes

The authors declare no competing financial interest.

■ ACKNOWLEDGMENTS

This research was supported by the National Natural Science Foundation of China (grant No. 42362019).

■ REFERENCES

(1) Wang, C.; Zhao, X.; Liu, Z.; Lippert, P.; Graham, S.; Coe, R.; Haisheng, Y.; Zhu, L.; Liu, S.; Li, Y. Constraints on early uplift history of the Tibetan Plateau. *Proc. Natl. Acad. Sci. U.S.A.* **2008**, *105*, 4987−4992.

(2) Zhu, D.-C.; Li, S.-M.; Cawood, P. A.; Wang, Q.; Zhao, Z.-D.; Liu, S.-A.; Wang, L.-Q. Assembly of the Lhasa and Qiangtang terranes in central Tibet by divergent double subduction. *Lithos* **2016**, *245*, 7−17.

(3) Wang, C.; Dai, J.; Zhao, X.; Li, Y.; Graham, S. A.; He, D.; Ran, B.; Meng, J. Outward-growth of the Tibetan Plateau during the Cenozoic: A review. *Tectonophysics* **2014**, *621*, 1−43.

(4) Yin, A.; Harrison, M. Geologic Evolution of the Himalayan-Tibetan Orogen. *Annu. Rev. Earth Planet. Sci.* **2000**, *28*, 211−280.

(5) Molnar, P.; Tapponnier, P. Cenozoic Tectonics of Asia: Effects of a Continental Collision: Features of recent continental tectonics in Asia can be interpreted as results of the India-Eurasia collision. *Science* **1975**, *189*, 419−426.

(6) Kapp, P.; DeCelles, P. G. Mesozoic−Cenozoic geological evolution of the Himalayan-Tibetan orogen and working tectonic hypotheses. *Am. J. Sci.* **2019**, *319* (3), 159−254.

(7) Fielding, E.; Isacks, B.; Barazangi, M.; Duncan, C. How flat is Tibet? *Geology* **1994**, *22*, 163−167.

(8) Xiong, Z.; Liu, X.; Ding, L.; Farnsworth, A.; Spicer, R.; Xu, Q.; Valdes, P.; He, S.; deng, Z.; Wang, C.; Li, Z.; Guo, X.; Su, T.; Zhao, C.; Wang, H.; Yahui, Y. The rise and demise of the Paleogene Central Tibetan Valley. *Sci. Adv.* **2022**, *8*, No. eabj0944.

(9) Mi, W.; Yang, W.; Zhu, L.; Wu, J.; Chen, A.; Huang, H. Source analysis and geological significance of Paleogene in southern Nima Basin, Tibet. *Tecton. Metallog.* **2018**, *42* (1), 177−192.

(10) Fang, X.; Dupont-Nivet, G.; Wang, C.; Song, C.; Meng, Q.; Weilin, Z.; Nie, J.; Zhang, T.; Ziqiang, M.; Chen, Y. Revised chronology of central Tibet uplift (Lunpola Basin). *Sci. Adv.* **2020**, *6*, No. eaba7298.

(11) DeCelles, P. G.; Kapp, P.; Ding, L.; Gehrels, G. E. Late Cretaceous to middle Tertiary basin evolution in the central Tibetan Plateau: Changing environments in response to tectonic partitioning, aridification, and regional elevation gain. *Geol. Soc. Am. Bull.* **2007**, *119* (5−6), 654−680.

(12) Han, Z.; Sinclair, H. D.; Li, Y.; Wang, C.; Tao, Z.; Qian, X.; Ning, Z.; Zhang, J.; Wen, Y.; Lin, J.; Zhang, B.; Xu, M.; Dai, J.; Zhou, A.; Liang, H.; Cao, S. Internal Drainage Has Sustained Low-Relief Tibetan Landscapes Since the Early Miocene. *Geophys. Res. Lett.* **2019**, *46* (15), 8741−8752.

(13) Mi, W.; Zhu, L.; Yang, W.; Yang, L.; Huang, H. The provenance and geological significance of the Paleogene Niubao Formation in the northern part of the Nima Basin, Tibet. *Earth Sci.* **2017**, *42* (02), 240−257 (In Chinese with abstract).

(14) Sun, J.; Li, J.; Liu, W.; Jin, C. A review of Cenozoic stratigraphic age, paleoenvironment and paleoheight studies in Lunpola Basin, central Tibetan Plateau. *Sci. Bull.* **2024**, *69* (18), 2463−2479.

(15) Song, B.; Zhang, K.; Wei, Y.; Jiang, G.; Yang, T.; Algeo, T. J.; Wang, J.; Han, F. Paleogene sediment provenance in the Gaize Basin: Implications for early Cenozoic paleogeography of central Tibet. *Palaeogeogr., Palaeoclimatol., Palaeoecol.* **2023**, *632*, No. 111860.

(16) Li, C.; Zhao, Z.; Lu, H.; Li, H. Late Mesozoic-Cenozoic multistage exhumation of the central Bangong-Nujiang Suture, Central Tibet. *Tectonophysics* **2022**, *827*, No. 229268.

(17) Han, X.; Dai, J.-G.; Lin, J.; Xu, S.; Liu, B.; Hu, T.; Zhang, C.; Wang, C.-S. An Oligocene-Miocene intermontane narrow lowland in the central Tibetan Plateau: Insights from provenance analysis and palynological record of a Cenozoic sedimentary succession. *J. Asian Earth Sci.* **2022**, *240*, No. 105438.

(18) Ding, L.; Xu, Q.; Yue, Y.; Wang, H.; Cai, F.; Li, S. The Andean-type Gangdese Mountains: Paleoelevation record from the Paleocene−Eocene Linzhou Basin. *Earth Planet. Sci. Lett.* **2014**, *392*, 250−264.

(19) Hu, F.; Wu, F.; Chapman, J. B.; Ducea, M. N.; Ji, W.; Liu, S. Quantitatively Tracking the Elevation of the Tibetan Plateau Since the Cretaceous: Insights From Whole-Rock Sr/Y and La/Yb Ratios. *Geophys. Res. Lett.* **2020**, *47* (15), No. e2020GL089202.

(20) Su, T.; Farnsworth, A.; Spicer, R. A.; Huang, J.; Wu, F.-X.; Liu, J.; Li, S.-F.; Xing, Y.-W.; Huang, Y.-J.; Deng, W.-Y.-D.; Tang, H.; Xu, C.-L.; Zhao, F.; Srivastava, G.; Valdes, P. J.; Deng, T.; Zhou, Z.-K. No high Tibetan Plateau until the Neogene. *Sci. Adv.* **2019**, *5* (3), No. eaav2189.

(21) Deng, L.; Jia, G. High-relief topography of the Nima basin in central Tibetan Plateau during the mid-Cenozoic time. *Chem. Geol.* **2018**, *493*, 199−209.

(22) Valdes, P. J.; Ding, L.; Farnsworth, A.; Spicer, R.; li, S.; Su, T. Comment on "Revised paleoaltimetry data show low Tibetan Plateau elevation during the Eocene. *Science* **2019**, *365*, No. eaax8474.

(23) Rohrmann, A.; Kapp, P.; Carrapa, B.; Reiners, P. W.; Guynn, J.; Ding, L.; Heizler, M. Thermochronologic evidence for plateau formation in central Tibet by 45 Ma. *Geology* **2012**, *40* (2), 187−190.

(24) Ding, L.; Kapp, P.; Cai, F.; Garzione, C. N.; Xiong, Z.; Wang, H.; Wang, C. Timing and mechanisms of Tibetan Plateau uplift. *Nat. Rev. Earth Environ.* **2022**, *3* (10), 652−667.

(25) Hetzel, R.; Dunkl, I.; Haider, V.; Strobl, M.; von Eynatten, H.; Ding, L.; Frei, D. Peneplain formation in southern Tibet predates the India-Asia collision and plateau uplift. *Geology* **2011**, *39* (10), 983−986.

(26) Pan, G.; Wang, L.; Li, R.; Yuan, S.; Ji, W.; Yin, F.; Zhang, W.; Wang, B. Tectonic evolution of the Qinghai-Tibet Plateau. *J. Asian Earth Sci.* **2012**, *53*, 3−14.

(27) Zhang, H.; Torsvik, T. Circum-Tethyan magmatic provinces, shifting continents and Permian climate change. *Earth Planet. Sci. Lett.* **2022**, *584*, No. 117453.

(28) Tang, M.; Ji, W.-Q.; Chu, X.; Wu, A.; Chen, C. Reconstructing crustal thickness evolution from europium anomalies in detrital zircons. *Geology* **2021**, *49* (1), 76−80.

(29) Yakymchuk, C.; Holder, R. M.; Kendrick, J.; Moyen, J.-F. Europium anomalies in zircon: A signal of crustal depth? *Earth Planet. Sci. Lett.* **2023**, *622*, No. 118405.

(30) Hu, P.-y.; Zhai, Q.-g.; Cawood, P. A.; Weinberg, R. F.; Zhao, G.-c.; Zhou, R.-j.; Tang, Y.; Liu, Y.-m. Detrital zircon REE and tectonic settings. *Lithos* **2024**, *480−481*, No. 107661.

(31) Yu, X.; Guo, Z. Surface uplift of the Tibetan Plateau: Constraints from isostatic effects of Cenozoic sedimentary accumulation. *J. Asian Earth Sci.* **2021**, *208*, No. 104662.

(32) Zhu, D.-C.; Zhao, Z.-D.; Niu, Y.; Dilek, Y.; Hou, Z.-Q.; Mo, X.-X. The origin and pre-Cenozoic evolution of the Tibetan Plateau. *Gondwana Res.* **2013**, *23* (4), 1429−1454.

(33) Royden, L. H.; Burchfiel, B.; van der Hilst, R. The Geological Evolution of the Tibetan Plateau. *Science* **2008**, *321*, 1054−1058.

(34) Kapp, P.; DeCelles, P. G.; Gehrels, G. E.; Heizler, M.; Ding, L. Geological records of the Lhasa-Qiangtang and Indo-Asian collisions in the Nima area of central Tibet. *Geol. Soc. Am. Bull.* **2007**, *119* (7−8), 917−933.

(35) Tong, K.; Li, Z.; Zhu, L.; Xu, G.; Zhang, Y.; Kamp, P. J. J.; Tao, G.; Yang, W.; Li, J.; Wang, Z.; Jiang, X.; Zhang, H. Thermochronology constraints on the Cretaceous-Cenozoic thermo-tectonic

evolution in the Gaize region, central-western Tibetan Plateau: Implications for the westward extension of the proto-Tibetan Plateau. *J. Asian Earth Sci.* **2022**, *240*, No. 105419.
(36) Wu, Z.; Zhang, Q.; Wu, Y.; Ye, P. Response of Paleogene sedimentary depression to crustal thickening in Selinco and adjacent areas of Tibet. *Acta Geol. Sin.* **2016**, *90* (09), 2181−2191.
(37) Kapp, P.; Murphy, M. A.; Yin, A.; Harrison, T. M.; Ding, L.; Guo, J. Mesozoic and Cenozoic tectonic evolution of the Shiquanhe area of western Tibet *Tectonics* 2003; Vol. *22* 4 DOI: 10.1029/2001TC001332.
(38) Luo, A.-B.; Fan, J.-J.; Sun, D.-Y.; Wu, H.; Yu, Y.-P.; Zhang, B.-C.; Shen, D. Terminal stage of divergent double subduction: Insights from Early Cretaceous magmatic rocks in the Gerze area, central Tibet. *Lithos* **2022**, *420*−*421*, No. 106713.
(39) Li, S.; Ding, L.; Guilmette, C.; Fu, J.; Xu, Q.; Yue, Y.; Henrique-Pinto, R. The subduction-accretion history of the Bangong-Nujiang Ocean: Constraints from provenance and geochronology of the Mesozoic strata near Gaize, central Tibet. *Tectonophysics* **2017**, *702*, 42−60.
(40) Kapp, P.; Yin, A.; Harrison, T. M.; Ding, L. Cretaceous-Tertiary shortening, basin development, and volcanism in central Tibet. *Geol. Soc. Am. Bull.* **2005**, *117* (7-8), 865−878.
(41) Wu, H.; Li, C.; Hu, P.; Zhang, H.; Li, J. Identification and geological significance of Early Cretaceous bipeak volcanic rocks in the Bangong-Nujiang Suture Zone, northern Tibet. *Geol. Bull.* **2014**, *33* (11), 1804−1814.
(42) Shi, L.-Z.; Huang, J.-Y.; Chen, W. Birth and demise of the Bangong−Nujiang Tethyan Ocean: A review from the Gerze area of Central Tibet: Comment. *Earth-Sci. Rev.* **2020**, *208*, No. 103209.
(43) Liu, Y.; Hu, Z.; Zong, K.; Gao, C.; Gao, S.; Xu, J.; Chen, H. Reappraisement and refinement of zircon U-Pb isotope and trace element analyses by LA-ICP-MS. *Chin. Sci. Bull.* **2010**, *55* (15), 1535−1546.
(44) Liu, Y.; Hu, Z.; Gao, S.; Günther, D.; Xu, J.; Gao, C.; Chen, H. In situ analysis of major and trace elements of anhydrous minerals by LA-ICP-MS without applying an internal standard. *Chem. Geol.* **2008**, *257* (1−2), 34−43.
(45) Liu, Y.; Gao, S.; Hu, Z.; Gao, C.; Zong, K.; Wang, D. Continental and Oceanic Crust Recycling-induced Melt-Peridotite Interactions in the Trans-North China Orogen: U-Pb Dating, Hf Isotopes and Trace Elements in Zircons from Mantle Xenoliths. *J. Petrol.* **2010**, *51* (1−2), 537−571.
(46) Reiners, P. W.; Brandon, M. T. Using Thermochronology to Understand Orogenic Erosion. *Annu. Rev. Earth Planet. Sci.* **2006**, *34* (1), 419−466.
(47) Foeken, J. P. T.; Stuart, F. M.; Dobson, K. J.; Persano, C.; Vilbert, D. A diode laser system for heating minerals for (U-Th)/He chronometry *Geochem., Geophys., Geosyst.* 2006; Vol. *7* 4 DOI: 10.1029/2005GC001190.
(48) Vermeesch, P.; Seward, D.; Latkoczy, C.; Wipf, M.; Günther, D.; Baur, H. α-Emitting mineral inclusions in apatite, their effect on (U−Th)/He ages, and how to reduce it. *Geochim. Cosmochim. Acta* **2007**, *71* (7), 1737−1746.
(49) Farley, K. A.; Wolf, R. A.; Silver, L. T. The effects of long alpha-stopping distances on (U-Th)/He ages. *Geochim. Cosmochim. Acta* **1996**, *60*, 4223−4229.
(50) Li, S.; Guilmette, C.; Ding, L.; Xu, Q.; Fu, J.-J.; Yue, Y.-H. Provenance of Mesozoic clastic rocks within the Bangong-Nujiang suture zone, central Tibet: Implications for the age of the initial Lhasa-Qiangtang collision. *J. Asian Earth Sci.* **2017**, *147*, 469−484.
(51) Li, C.; Wang, G. H.; Zhao, Z. B.; Du, J. X.; Ma, X. X.; Zheng, Y. L. Late Mesozoic tectonic evolution of the central Bangong−Nujiang Suture Zone, central Tibetan Plateau. *Int. Geol. Rev.* **2020**, *62* (18), 2300−2323.
(52) Li, S.; Yin, C.; Guilmette, C.; Ding, L.; Zhang, J. Birth and demise of the Bangong-Nujiang Tethyan Ocean: A review from the Gerze area of central Tibet. *Earth-Sci. Rev.* **2019**, *198*, No. 102907.
(53) Yu, X.; Guo, Z.; Fu, S. Endorheic or exorheic: differential isostatic effects of Cenozoic sediments on the elevations of the cratonic basins around the Tibetan Plateau. *Terra Nova* **2015**, *27* (1), 21−27.
(54) Rubey, W. W.; King Hubbert, M. Role of Fluid Pressure in Mechanics of Overthrust Faulting. *Geol. Soc. Am. Bull.* **1959**, *70* (2), 167−206.
(55) Sclater, J. G.; Christie, P. A. F. Continental stretching: An explanation of the Post-Mid-Cretaceous subsidence of the central North Sea Basin. *J. Geophys. Res.:Solid Earth* **1980**, *85* (B7), 3711−3739.
(56) Spiegel, C.; Kohn, B.; Belton, D.; Berner, Z.; Gleadow, A. Apatite (U−Th−Sm)/He thermochronology of rapidly cooled samples: The effect of He implantation. *Earth Planet. Sci. Lett.* **2009**, *285* (1−2), 105−114.
(57) Han, F.; Jiang, G.; Li, S.; Wei, Y.; Wang, J.; Song, B.; Zhang, K. Redefining the age attribution of continental facies red beds in the Mengdangle section of Gaize Basin, Tibet and its stratigraphic significance. *J. Stratigr.* **2022**, *46* (3), 286−305.
(58) Jordan, T.; Watts, A. Gravity anomalies, flexure and the elastic thickness structure of the India−Eurasia collisional system. *Earth Planet. Sci. Lett.* **2005**, *236* (3−4), 732−750.
(59) Yu, X.; Ji, J.; Wang, F.; Zhong, D. Intensified climate-driven exhumation along the South Himalayan Front since one million years ago. *J. Asian Earth Sci.* **2017**, *136*, 50−57.
(60) Yu, X.; Guo, Z. The role of base level, watershed attribute and sediment accumulation in the landscape and tectonic evolution of the Circum-Tibetan Plateau Basin and Orogen System. *J. Asian Earth Sci.* **2019**, *186*, No. 104053.
(61) Lu, L.; Zhen, Z.; Zhenhan, W.; Cheng, Q.; Peisheng, Y. Fission Track Thermochronology Evidence for the Cretaceous and Paleogene Tectonic Event of Nyainrong Microcontinent, Tibet. *Acta Geol. Sin. (Engl. Ed.)*. **2015**, *89* (01), 133−144.
(62) Lai, W.; Hu, X.; Garzanti, E.; Xu, Y.; Ma, A.; Li, W. Early Cretaceous sedimentary evolution of the northern Lhasa terrane and the timing of initial Lhasa-Qiangtang collision. *Gondwana Res.* **2019**, *73*, 136−152.
(63) Zhanli, R.; Junping, C.; Chiyang, L.; Tiejun, L.; Gang, C.; Shuang, D.; Tao, T.; Yating, L. Apatite Fission Track Evidence of Uplift Cooling in the Qiangtang Basin and Constraints on the Tibetan Plateau Uplift. *Acta Geol. Sin.* **2015**, *89* (02), 467−484.
(64) Zhao, Z.; Lu, L.; Wu, Z. Uplift evolution of the central uplift belt in the Qiangtang Basin: tectono-thermochronological constraints. *Front. Earth Sci.* **2019**, *26* (02), 249−263.
(65) Zhao, Z. B.; Bons, P. D.; Li, C.; Wang, G. H.; Ma, X. X.; Li, G. W. The Cretaceous crustal shortening and thickening of the South Qiangtang Terrane and implications for proto-Tibetan Plateau formation. *Gondwana Res.* **2020**, *78*, 141−155.
(66) Volkmer, J. E.; Kapp, P.; Horton, B. K.; Gehrels, G. E.; Minervini, J. M.; Ding, L.Northern Lhasa thrust belt of central Tibet: Evidence of Cretaceous−early Cenozoic shortening within a passive roof thrust system? *Special Paper of the Geological Society of America* 2014; Vol. *507*, p 507.
(67) Li, Y.; He, J.; Wang, C.; Santosh, M.; Dai, J.; Zhang, Y.; Wei, Y.; Wang, J. Late Cretaceous K-rich magmatism in central Tibet: Evidence for early elevation of the Tibetan plateau? *Lithos* **2013**, *160*−*161*, 1−13.
(68) Chen, S. S.; Fan, W. M.; Shi, R. D.; Gong, X. H.; Wu, K. Removal of deep lithosphere in ancient continental collisional orogens: A case study from central Tibet, China. *Geochem., Geophys., Geosyst.* **2017**, *18* (3), 1225−1243.
(69) Liu, Y.; Wang, M.; Li, C.; Li, S.; Xie, C.; Zeng, X.; Dong, Y.; Liu, J. Late Cretaceous tectono-magmatic activity in the Nize region, central Tibet: evidence for lithospheric delamination beneath the Qiangtang−Lhasa collision zone. *Int. Geol. Rev.* **2019**, *61* (5), 562−583.
(70) Lu, L.; Zhang, K.-J.; Jin, X.; Zeng, L.; Yan, L.-L.; Santosh, M. Crustal Thickening of the Central Tibetan Plateau prior to India−Asia Collision: Evidence from Petrology, Geochronology, Geochemistry and Sr−Nd−Hf Isotopes of a K-rich Charnockite−Granite Suite in Eastern Qiangtang. *J. Petrol.* **2019**, *60* (4), 827−854.

(71) Luo, A.-B.; Wang, M.; Zeng, X.-W.; Hao, Y.-J.; Li, H. An extensional collapse model for the Lhasa−Qiangtang orogen in Central Tibet. *Gondwana Res.* **2021**, *89*, 66−87.

(72) Wu, H.; Chen, J.; Wang, Q.; Yu, Y. Spatial and temporal variations in the geochemistry of Cretaceous high-Sr/Y rocks in Central Tibet. *Am. J. Sci.* **2019**, *319* (2), 105−121.

(73) Li, Y.; Wang, C.; Dai, J.; Xu, G.; Hou, Y.; Li, X. Propagation of the deformation and growth of the Tibetan−Himalayan orogen: A review. *Earth-Sci. Rev.* **2015**, *143*, 36−61.

(74) Li, Y.; Wang, C.; Zhao, X.; Yin, A.; Ma, C. Cenozoic thrust system, basin evolution, and uplift of the Tanggula Range in the Tuotuohe region, central Tibet. *Gondwana Res.* **2012**, *22* (2), 482−492.

(75) Fang, X. The uplift stage of the Tibetan Plateau. *Sci. Technol. Guide* **2017**, *35* (06), 42−50.

(76) Meng, J.; Wang, C.; Zhao, X.; Coe, R.; Li, Y.; Finn, D. India-Asia collision was at 24°N and 50 Ma: palaeomagnetic proof from southernmost Asia. *Sci. Rep.* **2012**, *2* (1), No. 925.

(77) Clark, M. K.; Royden, L. H. Topographic ooze: Building the eastern margin of Tibet by lower crustal flow *Geology* 2000; Vol. *28* 8.

(78) Wei, W.; Lu, Y.; Xing, F.; Liu, Z.; Pan, L.; Algeo, T. J. Sedimentary facies associations and sequence stratigraphy of source and reservoir rocks of the lacustrine Eocene Niubao Formation (Lunpola Basin, central Tibet). *Mar. Pet. Geol.* **2017**, *86*, 1273−1290.

(79) Xue, W.; Najman, Y.; Hu, X.; Persano, C.; Stuart, F. M.; Li, W.; Ma, A.; Wang, Y. Late Cretaceous to Late Eocene Exhumation in the Nima Area, Central Tibet: Implications for Development of Low Relief Topography of the Tibetan Plateau. *Tectonics* **2022**, *41* (3), No. e2021TC006989.

(80) Wei, Y.; Zhang, K.; Garzione, C. N.; Xu, Y.; Song, B.; Ji, J. Low palaeoelevation of the northern Lhasa terrane during late Eocene: Fossil foraminifera and stable isotope evidence from the Gerze Basin. *Sci. Rep.* **2016**, *6* (1), No. 27508.

(81) Song, E. *Clay Mineral Characteristics and Paleoclimate Environment Evolution of Sedimentary Strata in Gaize Basin, Central Tibetan Plateau. [D]*; China University of Geosciences, 2014.

https://doi.org/10.1021/acsomega.4c10175
ACS Omega 2025, 10, 22562−22575